This is a peer-reviewed, accepted author manuscript of the following research article: Zhang, Y, Zhao, X, Chen, K & Li, H 2025, 'Selecting projection views based on error equidistribution for computed tomography', Journal of X-Ray Science and Technology. https://doi.org/10.1177/08953996241289267

Selecting projection views based on error equidistribution for computed tomography

Yinghui Zhang[1,2], Xing Zhao[1], Ke Chen[2,3,⋆], Hongwei Li[1,⋆]

[1] School of Mathematical Sciences, Capital Normal University, Beijing 100048, China.

[2] Centre for Mathematical Imaging Techniques, University of Liverpool, Liverpool L69 7ZL, United Kingdom.

[3] Department of Mathematics and Statistics, University of Strathclyde, Glasgow, G1 1XH, United Kingdom.

[*] Corresponding author

Ke Chen. email: k.chen@strath.ac.uk,

Hongwei Li. email: hongwei.li91@cnu.edu.cn

Abstract

Background: Nonuniform sampling is a useful technique to optimize the acquisition of projections with a limited budget. Existing methods for selecting important projection views have limitations, such as relying on blueprint images or excessive computing resources.

Methods: We aim to develop a simple nonuniform sampling method for selecting informative projection views suitable for practical CT applications. The proposed algorithm is inspired by two key observations: projection errors contain angle-specific information, and adding views around error peaks effectively reduces errors and improves reconstruction. Given a budget and an initial view set, the proposed method involves: estimating projection errors based on current set of projection views, adding more projection views based on error equidistribution to smooth out errors, and final image reconstruction based on the new set of projection views. This process can be recursive, and the initial view can be obtained uniformly or from a prior for greater efficiency.

Results: Comparison with popular view selection algorithms using simulated and real data demonstrates consistently superior performance in identifying optimal views and generating high-quality reconstructions. Notably, the new algorithm performs well in both PSNR and SSIM metrics while being computationally efficient, enhancing its practicality for CT optimization.

Conclusions: A projection view selection algorithm based on error equidistribution is proposed, offering superior reconstruction quality and efficiency over existing methods. It is ready for real CT applications to optimize dose utilization.

Contents

I. **Introduction** **1**

II. **Methodology** **3**

II.A. The discrete imaging model of CT 4

II.B. The high correlation between informative projection angles and edges' angular orientation 4

II.C. Motivation: the behaviors of the projection error curve 5

II.D. The proposed PVSEE 9

III. **Experiments** **11**

III.A. Effectiveness validation of the proposed PVSEE 12

III.A.1. Scanned object with preferential directions 12

III.A.2. Scanned object without preferential directions 14

III.B. Performance evaluation of the proposed PVSEE 15

III.B.1. Performance test on simulated data 16

III.B.2. Performance test on real data 22

IV. **Discussion** **27**

IV.A. The initial set of projection views 27

IV.B. The recursive variant of PVSEE method 29

IV.C. The application scenarios 31

V. **Conclusion** **31**

References **33**

I. Introduction

Thanks to its non-evasiveness, high resolution, and good flexibility, X-ray computed tomography (CT) is a popular imaging technique that has been extensively used for medical imaging, non-destructive testing (NDT), material characterization, etc. By reconstructing tomographic images from X-ray measurements for a number of scanning angles (views), CT reveals the inner structures of scanned objects.

Conventionally, the scanning views are equally distributed in a specific angular range, and to achieve high quality reconstructions, the number of scanning views should meet certain sampling constraint[1,2]. This might be inappropriate for applications like medical examinations where too much X-ray radiations could result in health risks[3,4]. Even in industrial applications, high radiation dose leads to increased costs and decreased detection efficiency[5,6]. Numerous methods have been developed to optimize dose utilization. Yu et al.[7] summarized the general technical strategies that are commonly used for radiation dose management in CT, including CT system optimization, reducing scanning range, automatic exposure control, optimal tube potential and noise control strategies in reconstruction and data processing, etc.

One effective approach to reducing radiation exposure is to minimize the number of projections required for image reconstruction. This raises the problem: how to select the most "valuable" projection views ? Previous studies have highlighted the crucial influence of projection view selection[8–12]. For instance, in[8], I.G. Kazantsev demonstrated that it is possible to identify an angle distribution that maximizes the information content about the scanned object to significantly improve the reconstruction quality.

In order to determine the most informative set of projection angles, numerous nonuniform angular sampling methods have been proposed over the past few decades. Placidi et al.[13] introduced an adaptive method that selects projections based on the principle of "entropy". This adaptive scheme effectively reduces the required number of projections when the scanned object exhibits internal symmetries. Venere et al.[14] exploited the preferential direction of elliptical-shaped cracks and demonstrated that the preferred projection views should align with the main axis of the ellipse. Later, motivated by E. Quinto's visible and invisible edges principle[15], Zheng and Mueller[16,17] developed a method for selecting the most relevant projections that contain rays tangent to salient edges of the scanned object. Haque et al[18] proposed to select the projection angles based on the spectral richness of the acquired projections. Batenburg et al.[19,20] selected the next new angle by maximizing the information gained by adding each projection view. Similarly, by applying sequential feature selection (SFS) based on a blueprint image, Peter et al.[21] proposed to sequentially find the optimal angles with the highest information content measured by global uncertainty or relative mean error against the projections already acquired. These two methods suffer from high computational burden since they have to run the reconstruction algorithms many times to determine the next best angle. Recently, Victor Bussy et al.[22] extended the discrete empirical interpolation method (DEIM) and the reduced-order model to select the most informative and relevant projections. Joseph and Keng[23] proposed an IntelliScan approach that uses prior object information to select projections that contain X-rays tangent to the scanned object's surfaces. These works show that the informative projection views should align with the edges distribution of the object under scanning.

Inspired by the success of deep learning methods, neural networks have also been employed for angle selection. Shen et al.[24] used modern reinforcement learning methods to select projection angles and specify their doses for personalized scanning, where the CT scanning process is formulated as a Markov Decision Process. A one-step deep learning framework was proposed in[25] which can select the most related projection angles and learn a high-performance reconstruction network. Due to high computational burden, deep learning methods are mainly of research interest rather than application.

Despite the promising results achieved, existing methods suffer from applicability issues. Indeed, the aforementioned methods either need prior blueprint image (CAD model) to provide salient edges information, or perform some kind of brute-force searching hence consuming too much computational resources. In this paper, we design an effective and light-weight projection view selection approach that keeps applicability in mind. Given a set of projection views and a forward projection model, the projection error for each view is defined as the difference between the projection data and the corresponding scanned data quantified by some chosen metric. Our approach is inspired by two key observations for the behaviors of the projection errors during iterative reconstructions.

- The projection error for each projection angle carries information about the informativeness of that particular projection angle, i.e. projection errors effectively quantifies the importance of the corresponding projection angles.

- The addition of projection angles around the peaks of the (discrete) projection error curve, which is defined in Section II.C., effectively reduces projection errors and improves reconstruction quality.

Based on the above two observations, the goal is then to design a strategy for acquiring additional projection views around the peaks of the projection error curve. Fortunately, we find that the idea of error equidistribution just aligns with this objective. Error equidistribution[26,27] is a commonly used technique for adaptive spatial mesh design[28–30]. We borrow its basic idea for projection views selection by following the principle that each area under adjacent views on the error curve should be equal. This strategy guarantees more projection angles around the large projection errors are selected, thus a more informative set of projection views are determined.

The remainder of this paper is organized as follows. In Section II. , we describe the proposed projection view selection algorithm in detail, and numerical experiments shall be performed in Section III. to verify the effectiveness and efficiency of the proposed algorithm. We present discussions in Section IV. to address practical issues, and conclude our paper in V..

II. Methodology

This section provides a detailed description of the proposed projection views selection algorithm based on error equidistribution, which is named PVSEE here and after. We will first illustrate the high correlation between informative projection angles and the orientation of the object's edges. We then explain the motivation behind our proposed PVSEE algorithm. PVSEE essentially consists of three steps: projection error estimation, projection selection based on error equidistribution, and final image reconstruction. These three steps will be described in this section in detail.

II.A. The discrete imaging model of CT

Let's first introduce the notations used throughout the paper. The CT reconstruction problem could be formulated as solving a linear system,

$$Au = p \tag{1}$$

where $A = (a_{ji})_{J\times I}$ is the system matrix, $J = V \times D$ denotes the total number of rays, V and D denote the number of projection views and the number of detector cells, respectively, u is the reconstructed image of size $N_x \times N_y$, and $I = N_x \times N_y$ denotes the total number of image pixels.

For convenience, we use the subscript $[i]$ to refer to the i-th projection view, i.e. $A_{[i]}$ and $p_{[i]}$ refer to the projection operator (system matrix) and the projection data for the i-th view, respectively, such that

$$A = \begin{pmatrix} A_{[1]} \\ \vdots \\ A_{[i]} \\ \vdots \\ A_{[V]} \end{pmatrix}, p = \begin{pmatrix} p_{[1]} \\ \vdots \\ p_{[i]} \\ \vdots \\ p_{[V]} \end{pmatrix},$$

where $A_{[i]} \in \mathbb{R}^{D\times I}$ and $p_{[i]} \in \mathbb{R}^{D\times 1}$, for each $i \in \{1, 2, \dots, V\}$. For nonuniform distributed projection views, we refer to the ith view with its projection angle θ_i when necessary, i.e. $A_{[i]} = A_{\theta_i}$, and $p_{[i]} = p_{\theta_i} = (p_{\theta_i,1}, p_{\theta_i,2}, \cdots, p_{\theta_i,D})^T$.

II.B. The high correlation between informative projection angles and edges' angular orientation

When the scanned object exhibits preferential "directions", the most informative projection views will align with the principle directions of the edges[8,31,32]. To illustrate the high correlation between informative projection angles and edges' angular orientation , we present two reconstructions of the rectangle phantom shown in Fig. 1, with uniform and nonuniform samplings for the scanning angles, respectively. The reconstructed images, which are obtained by performing 10 iterations of the OS-SART algorithm, are illustrated in Fig. 1. The reconstruction with 6 projection angles uniformly distributed in $[0, \pi)$ is shown in Fig. 1(b) while the reconstruction with nonuniform spaced projections at angles $\{179°, 0°, 1°, 89°, 90°, 91°\}$

is shown in Fig. 1(d). It can be clearly seen that the reconstruction from uniformly spaced projections exhibits severe streak artifacts and blurring, while the reconstruction with the designed nonuniformly spaced projection angles does not suffer from streaks or blurring.

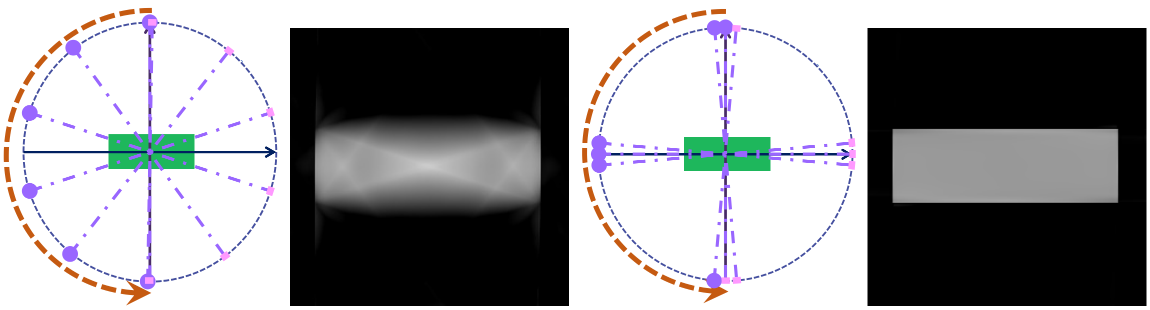

(a) (b) (c) (d)

Figure 1: (a) Diagram of uniform scanning, (b) Reconstruction from uniformly spaced projections, (c) Diagram of nonuniform scanning, (d) Reconstruction from nonuniformly spaced projections.

It is worth noting that the nonuniform angle distribution with the reconstruction shown in Fig. 1(d) aligns well with the main orientations of the rectangle, i.e. the scanning views are concentrated around $0°$ and $90°$. This coincides well with the visible and invisible edges theory developed by Quinto et.al[15]. So, if one knows the edges' distribution of the object before scanning, the projection views could be specified around the primary directions of the edges to achieve better reconstructions. In reality, however, the edges, especially the inner edges, are not known before reconstruction, so we need to find a way to draw the edges information during the reconstruction process, which is the main focus of our paper. Our method is based on two key observations about the correlations between the informativeness of projection angles and the projection error curve.

II.C. Motivation: the behaviors of the projection error curve

Recall the denotations described in section II.A., for a given image u, define the residual $e = p - Au$ and $e_{[i]} = p_{[i]} - A_{[i]}u$. Utilizing the above symbols, we could define the so-called projection error curve. Let

$$\mathcal{E}(\theta_i; e_{[i]}) = ||e_{[i]}||, i = 1, 2, \ldots, V, \tag{2}$$

where $\|\cdot\|$ denotes some chosen vector norm. Then the (discrete) projection error curve is defined as the set

$$\{(\theta_i, \mathcal{E}_i), i = 1, 2, \ldots, V\},$$

where $\mathcal{E}_i = \mathcal{E}(\theta_i; e_{[i]})$. So, the projection error curve is just a discrete function defined on the projection angles, hence it can be referred to as $\mathcal{E}(\theta) = (\mathcal{E}_1, \mathcal{E}_2, \ldots, \mathcal{E}_V)$ for simplicity, where V denotes the total number of views considered. Here, we always assume **the angles θ_i are sorted in ascending order**. In all our tests, the $\|\cdot\|_p$ norm is used to calculate the error curves. In fact, we have tested other choices like entropy and Kullback-Leibler (KL) divergence, all works about equally well.

For later reference, let's define the "continuous" projection error curve as

$$\mathcal{T}_{\#}\mathcal{E}(\theta) = \text{Linear Interpolation of } \mathcal{E}(\theta).$$

When it's clear from the context, we just use error curve to refer either the discrete error curve or it's continuous counterpart.

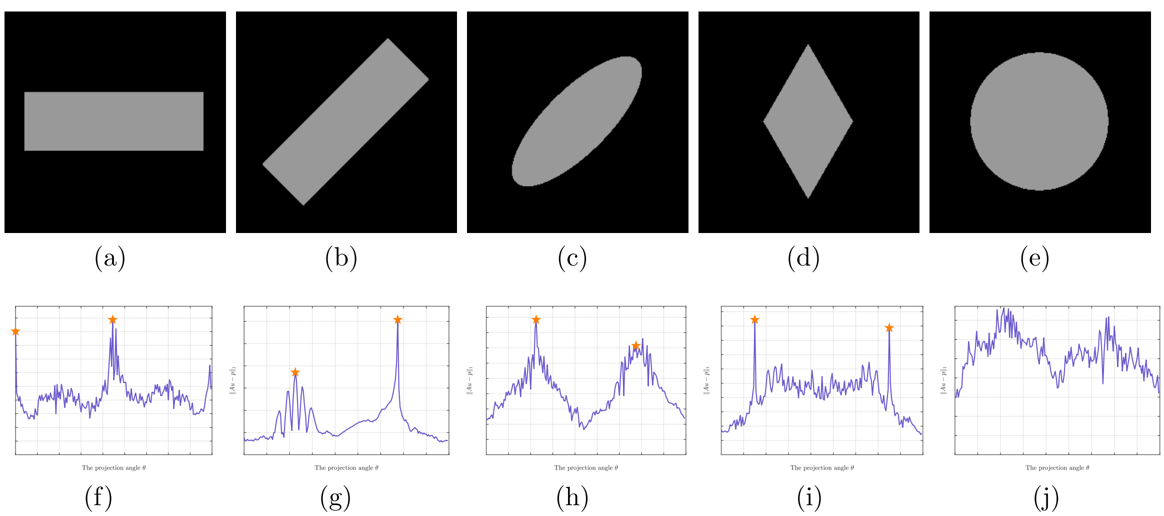

Figure 2: The correlations between projection errors and main orientations for the scanning objects. (a) Rectangle, (b) 45° anti-clockwise rotated rectangle, (c) 45° clockwise rotated ellipse, (d) Rhombus (with sides at 30° and 150°), (e) Circle, and (f)-(j) show projection error curves for (a)-(e), respectively.

Observation 1: Projection error can serve as a viable measure of projection angle importance. As shown in Fig. 2, five simple phantoms (size of 256 × 256) with varying shapes and primary orientations ((a)-(e)) are scanned with 180 projection views uniformly distributed in the full-range $[0, \pi)$. The SART algorithm (10 iterations) is then utilized to transform the acquired projection data p into the corresponding image u, and the projection error curve is then computed as

$$\mathcal{E}(\theta) = \{||e_{[i]}||_1, i = 1, 2, \ldots, V = 180\}, e_{[i]} = p_{[i]} - A_{[i]}u. \tag{3}$$

The second row of Fig. 2 depicts the projection error curves for each reconstruction. It's easy to see that, the peaks of the projection error curve, indicated by yellow stars, align well with the primary directions of the objects. This suggests that the projection errors could serve as the measure of the importance of projection angles since they have strong correlations with the primary directions of the object's edges.

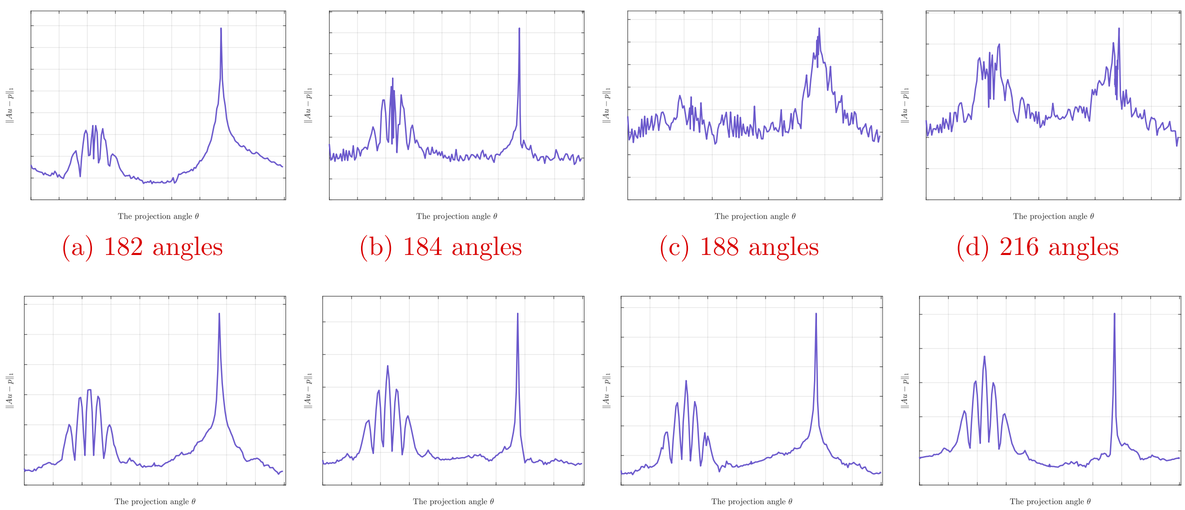

(a) 182 angles (b) 184 angles (c) 188 angles (d) 216 angles

(e) 182 angles (f) 184 angles (g) 188 angles (h) 216 angles

Figure 3: The effects of adding projection angles around the main orientations $\{45°, 135°\}$ against non-main orientations $\{0°, 90°\}$. The original projection error curve is calculated with 180 uniformly distributed projection views, and the added projection views are allocated around the orientations symmetrically, which are specified at: (a) $\{45.5°, 135.5°\}$, (b) $\{44.5°, 45.5°, 134.5°, 135.5°\}$, (c) $\{44° + i * 0.4°, 45° + i * 0.4°, 134° + i * 0.4°, 135° + i * 0.4°\}_{i=1}^{2}$, (d) $\{44° + i * 0.1°, 45° + i * 0.1°, 134° + i * 0.1°, 135° + i * 0.1°\}_{i=1}^{9}$. (e) $\{0.5°, 90.5°\}$, (f) $\{179.5°, 0.5°, 89.5°, 90.5°\}$, (g) $\{179° + i * 0.4°, 0° + i * 0.4°, 89° + i * 0.4°, 90° + i * 0.4°\}_{i=1}^{2}$, (h) $\{179° + i * 0.1°, 0° + i * 0.1°, 89° + i * 0.1°, 90° + i * 0.1°\}_{i=1}^{9}$.

Observation 2: Adding projection angles around the peaks of the projection error curve efficiently improves reconstruction quality.

If we want to improve the reconstruction quality by investing more projection views, where should these projection views go? Since the projection error curve indicates the importance of projection angles, a natural idea is to place these additional projection views around the peaks of the error curve. We consider for example the test with the 45° anti-clockwise arranged rectangle shown in Fig. 2(b). To demonstrate the effectiveness of adding projection views around the peaks of the projection error curve, i.e. in the vicinity of the main directions $\{45°, 135°\}$, two group of tests: one is to invest more and more projection views around $\{45°, 135°\}$, while the other group is to inject more and more projection views around $\{0°, 90°\}$, are performed to compare with each other. The original set of the projection views includes 180 uniformly distributed projection angles.

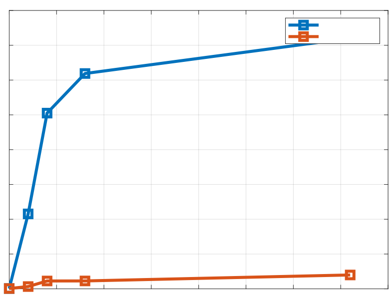

(a) PSNR

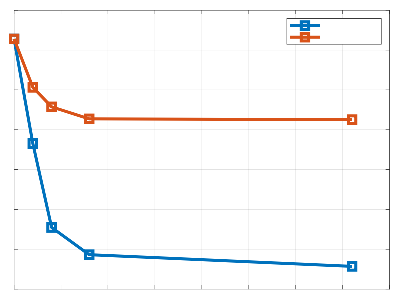

(b) Average projection errors

Figure 4: Performance comparison for adding projection views around the main orientations and non-main orientations, i.e. in the vicinity of $\{45°, 135°\}$ and $\{0°, 90°\}$. (a) PSNR values against numbers of projection views, (b) Average projection errors against number of projection views.

We monitor the development of the projection error curves with the added projection views, as displayed in Fig. 3. Fig. 3(a) - Fig. 3(d) in the first row illustrate the projection error values under adding more and more projection views around the peaks of the error curve, while Fig. 3(e)- Fig. 3(h) show the changing trends of the projection error curve during investing more and more projection views around the non-main orientations of the rectangle, i.e. far-away from the peaks of the error curves. For a fair comparison, both groups of tests take the same strategy for adding projection views. For the first group of tests, the added views are allocated symmetrically about $\{45°, 135°\}$, while for the second group of tests, they are symmetrically allocated about $\{0°, 90°\}$. Specifically, for the first group of tests, the added projection views are $\{45.5°, 135.5°\}$, $\{44.5°, 45.5°, 134.5°, 135.5°\}$, $\{44°+i*0.4°, 45°+i*0.4°, 134°+i*0.4°, 135°+i*0.4°\}_{i=1}^{2}$ and $\{44°+i*0.1°, 45°+i*0.1°, 134°+i*0.1°, 135°+i*0.1°\}_{i=1}^{9}$, while for the second group of tests, the added projection views are

$\{0.5°, 90.5°\}$, $\{179.5°, 0.5°, 89.5°, 90.5°\}$, $\{179°+i*0.4°, 0°+i*0.4°, 89°+i*0.4°, 90°+i*0.4°\}_{i=1}^{2}$ and $\{179°+i*0.1°, 0°+i*0.1°, 89°+i*0.1°, 90°+i*0.1°\}_{i=1}^{9}$. From these projection curves, we can see that the resulting projection error curves maintain their original shapes. Besides, the errors witness a significant drop from [0.5, 4] to [0.18, 0.54] when adding projection views around the peaks, while the errors only show a small fall from [0.5, 5.8] to [0.5, 5.1] when adding the projection views far away from the peaks. We also calculate the average projection errors and peak signal-to-noise ratio (PSNR)[33] of the reconstructed results which are then illustrated in Fig. 4. As observed, adding projection views around the peaks of the error curve can dramatically reduce error and significantly improve reconstruction quality compared with the case of adding projection views far away from the peaks.

II.D. The proposed PVSEE

Based on the insights gained from the above observations, this subsection focuses on the development of an adaptive algorithm for projection view selection. The proposed algorithm compromises two fundamental components, which leverage the findings of **Observation 1** and **Observation 2**. Taking **Observation 1** into account, we propose that the projection error can be used as a metric to evaluate the informativeness of the projection views. Considering **Observation 2**, to effectively reduce projection error and improve reconstruction quality, we propose to invest more projection views around the large projection errors and vice versa. To achieve the above goal, we employ the error equidistribution technique originally developed for mesh adaption[27] to flatten out the projection error curve by fulfilling the requirement that the areas between adjacent projection views on the error curve are all equal. This area equidistribution procedure effectively leads to error equidistribution by placing more projection views around the large values on the projection error curve.

Given the object to be scanned, the budget for the number of projection views V, and an initial set of M projection views, we now describe the PVSEE algorithm in detail. The proposed PVSEE for selecting $V - M$ informative projection views consists of three steps:

Step 1: **Projection error estimation**: Given an initial set of M projection views at angles $\{\theta_i\}_{i=1}^{M}$, reconstruct them into a rough estimation $\hat{u}$ for the scanned object by applying some reconstruction algorithm (operator), and then calculate the projection error curve $\{(\theta_i, \mathcal{E}_i)\}_{i=1}^{M}$.

Step 2: **Projection view selection following the error equidistribution law**: Given the projection error $\{\mathcal{E}_i\}_{i=1}^M$ on the present views $\{\theta\}_{i=1}^M$ from Step 1 , we now determine new $V-M$ projection views such that the projection error is (approximately) equidistributed. Let's denote the new added set of projection views as $\{\theta'_j\}_{j=1}^{V-M}$. The error equidistribution law specifies the added views as follows:

$$\begin{aligned} &\theta'_1 = \theta_1 \\ &\int_{\theta'_{j-1}}^{\theta'_j} \mathcal{T}_\# \mathcal{E}(\theta) d\theta = \frac{S}{V-M}, j = 2, \ldots, V-M. \end{aligned} \tag{4}$$

where $S = \int_{\theta_1}^{\theta_M} \mathcal{T}_\# \mathcal{E}(\theta) d\theta$.

Step 3: **Final image reconstruction**: Conduct CT scans at the new selected projection angles $\{\theta'_i\}_{i=1}^{V-M}$ obtained from Step 2, and then perform image reconstruction by applying the chosen **Reconstruction** operator on the obtained projection data for views

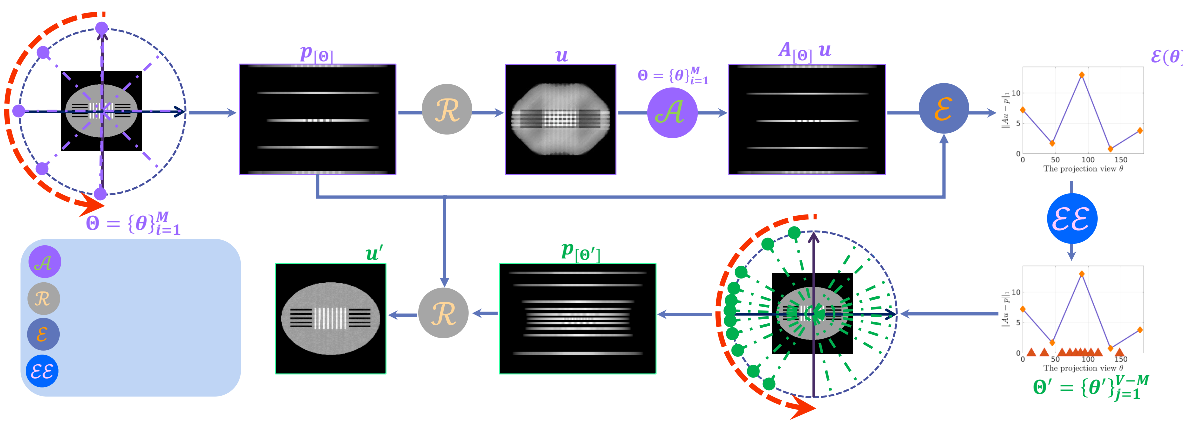

Figure 5: Schematic diagram of the projection view selection based on error equidistribution ($M = 5$, $V = 15$).

The whole process of proposed PVSEE is summarized as **Algorithm 1**, which is also illustrated in the schematic diagram shown in Fig. 5 for a special case ($M = 5$, $V = 15$). In this paper, we use MLEM-TV described in[18] to implement the **Reconstruction** operator. Please note that the choice of **Reconstruction** operator is not unique, other reconstruction algorithms could work equally well.

Algorithm 1: PVSEE

Input: Initial M views $\{\theta_i\}_{i=1}^{M}$, the number of target projection views V

Initialize: $\Theta \leftarrow \{\theta_i\}_{i=1}^{M}$

\# **Step 1**: estimate the projection error

Acquiring the projection data $p_{[\Theta]}$ for the views in Θ

Performing image reconstruction from projection data $p_{[\Theta]}$ by
$u \leftarrow$ **Reconstruction**$(p_{[\Theta]})$

Estimating the projection errors and generating the error curve $\mathcal{E}(\theta)$ by applying (3).

\# **Step 2**: select new $V - M$ projection views $\Theta' = \{\theta'_j\}_{j=1}^{V-M}$ by applying the error equidistribution law (4)

\# **Step 3**: achieve the final reconstruction

Including the selected views Θ' into the set of initial set of projection views by
$\Theta = \Theta \cup \Theta'$

Acquiring new projection data $p_{[\Theta']}$ for selected views in Θ'

Performing image reconstruction by
$u' \leftarrow$ **Reconstruction**$(p_{[\Theta]})$

Output: u'

III. Experiments

In this section, we will assess the performance of our proposed projection view selection algorithm. We have chosen four well-established projection selection schemes as our comparative methods: DEIM[22], SFS[21], dynamic angle selection[19], and adaptive projection selection based on spectral richness[18]. For easier reference, the last two methods shall be termed **"Dynamic"** and **"Spectral"**, respectively. Similarly, the uniform sampling scheme shall be named **"Uniform"**. The first two methods are used to validate the effectiveness of the proposed projection views selection strategy, while the last two methods are utilized to evaluate the performance of **Algorithm 1**. We have configured the parameters for these methods according to the guidelines provided in their original publications. Our evaluation will cover simulated and real data with and without preferential directions, taking both parallel beam and fan beam setups into account. The **Reconstruction** operator involves forward and backward projections which shall be implemented using the astra toolbox[34]. To draw quantitative conclusions, we will calculate quality metrics including Peak Signal-to-Noise Ratio (PSNR) and Structural Similarity Index Measurement (SSIM)[35]. When needed, Poisson noise specified by the incident intensity, denoted as I_0, will be introduced to the projection data p, i.e.

$$p_{\text{noisy}} = -\ln\left(\frac{\text{Poissrnd}(I_0) \times \exp(-p)}{I_0}\right), \tag{5}$$

where p and p_{noisy} denote noise-free and noisy projection data, respectively.

III.A. Effectiveness validation of the proposed PVSEE

In this subsection, the proposed PVSEE method will be tested against DEIM and SFS, two existing projection views selecting methods that assuming the availability of a blueprint image for the scanned object. The tests will be performed on two types of simulated phantoms, including the PCB (512×512)[36] which exhibits strong directional characteristics, and concentric circles (512×512) which exhibits no directional characteristics. We assume that full angle projections have already been acquired such that the projection selection task boils down to sparse sampling problem, involving the selection of $V^\dagger$ highly informative projections from $M^\dagger$ full-angle projections. It should be pointed out that the discrete phantom and reconstructed images of the PCB are originally size of 512×512, but have been clipped to the size of 196×422 for visual clarity.

III.A.1. Scanned object with preferential directions

In this first test, we use a simulated PCB phantom with preferential directions, as displayed in Fig. 6(a). The scanning geometry is configured as follows: parallel beam source, 1024 detector units with a unit length of 0.2mm. The noise level is set to $I_0 = 1 \times 10^6$. The phantom exhibits preferential directions of 0° and 90°. For this test, 30 views shall be selected from 180 full-angle uniform spacing angles.

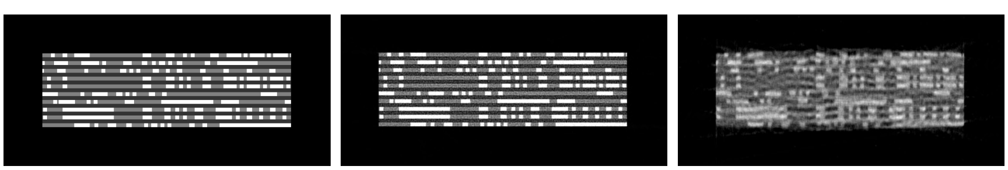

(a) Phantom (b) SART, full data (c) SART, sparse-view data

Figure 6: (a) The simulated PCB phantom, (b) Full angle SART reconstruction (10 iterations, noisy), (c) SART reconstruction from 30 views (10 iterations, noisy). The grayscale window is set to [0, 1].

Reconstructed results from projections by the proposed algorithm and comparative algorithms from noisy data are shown in Fig. 7. Thanks to more attention paid on the vicinity of the projection view 90°, the reconstructed results from projections selected by all schemes show better-recovered horizontal edges than that of the uniform scheme as shown in Fig. 7(a). When examining the zoomed-in images shown in Fig. 7(e)-(h), one can see that SFS and the proposed PVSEE demonstrate superiority since they suffer from much less artifacts. From quantitative indices shown in Table 1, we can see that the proposed PVSEE are better than DEIM, and comparable with SFS. It should be noted that SFS uses the information obtained at each additional angle to guide the selection of the next measurement, which makes it very slow as it has to execute the reconstruction algorithm multiple times to determine the best next angle. We monitor the runtime of competing algorithms computed with a single GTX 2080Ti GPU. As displayed in the bottom row of Table 1, SFS takes approximately 36 hours to select 30 angles out of 180 candidate angles, which is beyond endurance even though it gives slight better quantitative measures.

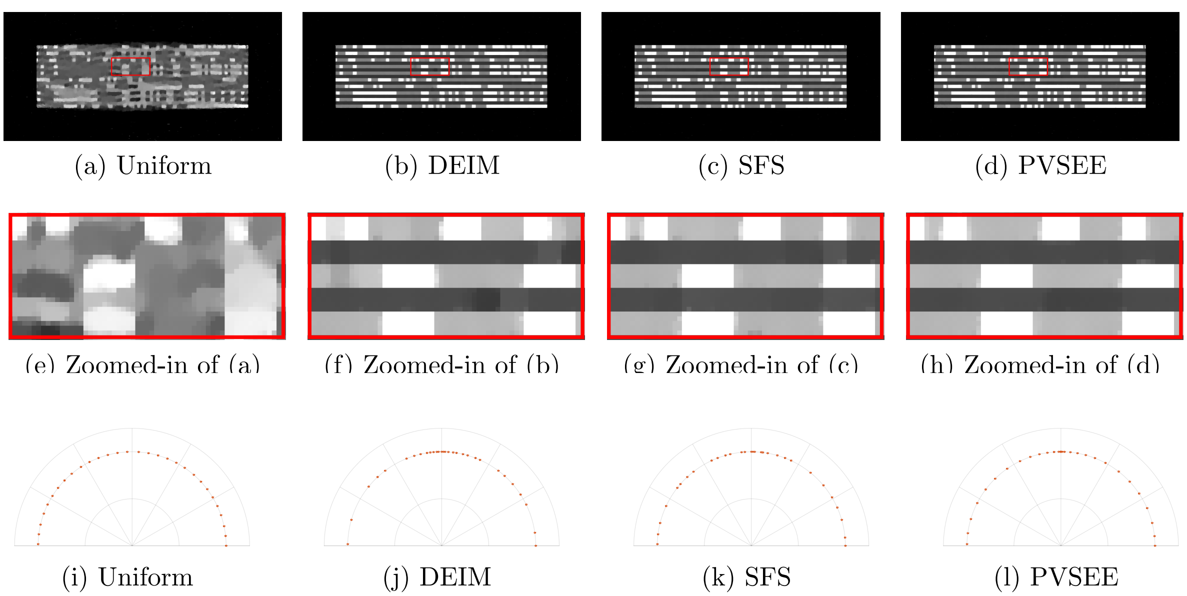

Figure 7: Results of projection view selection methods for PCB phantom from noisy projections ($M^{\dagger} = 180, V^{\dagger} = 30$). The display windows for the first row and the second row are set to $[0, 1]$ and $[0, 0.7]$.

Table 1: Quantitative evaluation (PSNR, SSIM and runtime) of projection view selection for the simulated PCB phantom on noisy projections.

Phantom	Index	Uniform	DEIM	SFS	PVSEE
PCB	PSNR	21.04	39.64	**42.54**	41.99
512 × 512	SSIM	0.8572	0.9881	0.9880	**0.9887**
	Running time(s)	20.56	20.94	130722.38	61.49

III.A.2. Scanned object without preferential directions

The second test is performed on a synthesized image of several circular rings, as illustrated in Fig. 8(a). This phantom shares the same scanning parameters as those with the previous test. Noisy projections are obtained by adding Poisson noise with incident photons of 1×10^5 to the noise-free data. Considering the symmetric structure of the phantom, which is quite simple, all competing algorithms are required to select 10 projection views from full-angle uniform spacing angles. The results are shown in Fig. 9. From the first line of Fig. 9, we

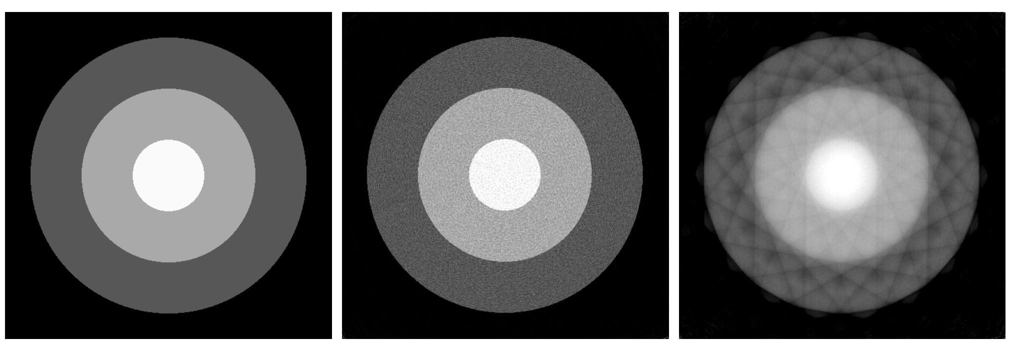

(a) Phantom (b) SART, full data (c) SART, sparse-view data

Figure 8: (a) The concentric circles phantom, (b) Full angle SART reconstruction (10 iterations, noisy), (c) SART reconstruction from 10 views (10 iterations, noisy). The grayscale window is set to [0, 0.8].

see that DEIM introduces obvious artifacts, SFS suffers from slight streak artifacts tangent to circles boundaries, while both the proposed PVSEE algorithm and the uniform spacing scheme produce similar much better reconstructions. The second line illustrates the selected projection angles. Clearly, PVSEE produces desirable near uniform projection angles, while DEIM and SFS result in quite non-uniform spaced angles. Since the phantom is central symmetric and no preferential directions, uniformly distributed projection views should be optimal, which could also be validated by the superior reconstruction from the uniform spacing scheme shown in Fig. 9(a). The advantages of the error equidistribution procedure

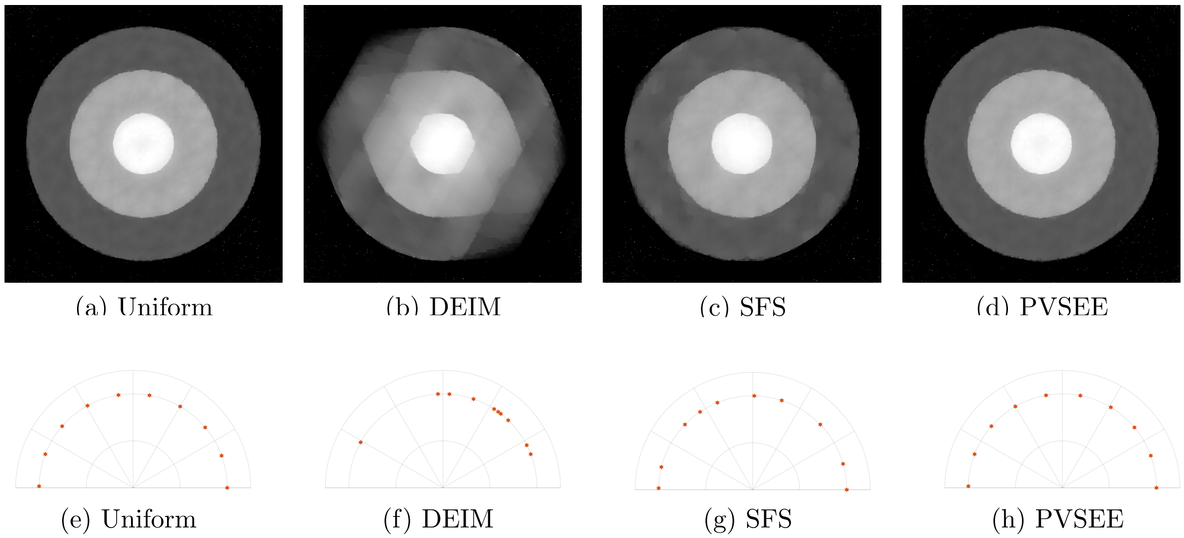

Figure 9: Results of projection view selection methods for concentric circles phantom from noisy projections ($M^\dagger = 180$, $V^\dagger = 10$). The grayscale window is set to [0, 0.8].

could be further verified by checking the quantitative indices listed in Table 2. Our PVSEE method demonstrates significant higher PSNR and SSIM. As for the running time, SFS takes too long to be practically useful. DEIM consumes about half time of that of PVSEE, however, its PSNR and SSIM values are much lower which makes it not comparable to the proposed PVSEE, in terms of quality.

Table 2: Quantitative evaluation (PSNR, SSIM and runtime) of projection view selection for the concentric circles phantom on noisy projections.

Phantom	Index	Uniform	DEIM	SFS	PVSEE
Concentric circles	PSNR	31.53	25.66	29.98	**31.54**
512×512	SSIM	0.9320	0.8851	0.9218	**0.9311**
	Runtime(s)	18.22	18.90	26373.62	37.81

III.B. Performance evaluation of the proposed PVSEE

In this subsection, the proposed PVSEE method will be tested against two popular methods: dynamic (dynamic angle selection) and spectral (adaptive projection selection based on spectral richness). To demonstrate deeper behaviors of the proposed method, comprehensive tests shall be performed with both simulated and real data, with and without preferential directions, and parallel and fan-beam X-ray sources.

III.B.1. Performance test on simulated data

The first test uses a simulated strips phantom, consisting of eight horizontal strips and seven vertical strips within an ellipse, as shown in Fig. 10(a). Like the previous test, this phantom is scanned using parallel-beam X-rays. The scanning configuration involves 512 detector units, each with a length of 0.2 mm. Noisy projections are generated by introducing Poisson noise with noise level $I_0 = 1 \times 10^6$ to the noise-free data. This phantom exhibits strong preferential directions $\{0°, 90°\}$. The original projection views set consists of $M = 15$ uniformly spaced angles, which is then expanded to $V = 30$ projection views by applying the views selection algorithms. Since there exists preferential directions $\{0°, 90°\}$, a good

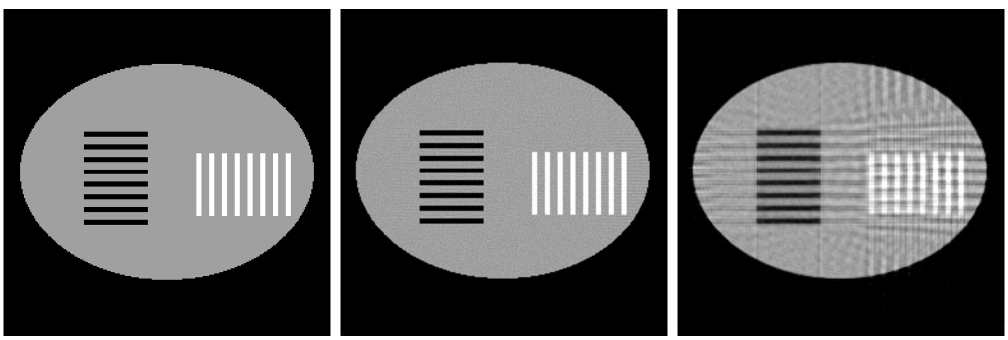

(a) Phantom (b) SART, full data (c) SART, sparse-view data

Figure 10: (a) The Strips phantom, (b) Full angle SART reconstruction (10 iterations, noisy), (c) SART reconstruction from 30 views (10 iterations, noisy). The grayscale window is set to [0, 1].

projection views selection scheme should determine more projections in the vicinity of 0° and 90°. The reconstructed results illustrated in Fig. 11(a)-(d) show that the competing algorithms Uniform, Dynamic, and Spectral bring obvious artifacts, while the proposed PVSEE algorithm produces high quality reconstruction, free of artifacts. When checking the selected projection views illustrated in Fig. 11(e)-(h), it's easy to see that only the proposed PVSEE algorithm selects more projection views around 90°, while all competing algorithms fail to do so. This explains off the superiority of PVSEE. The quantitative measurements listed in Table 3 agree well with the above conclusion.

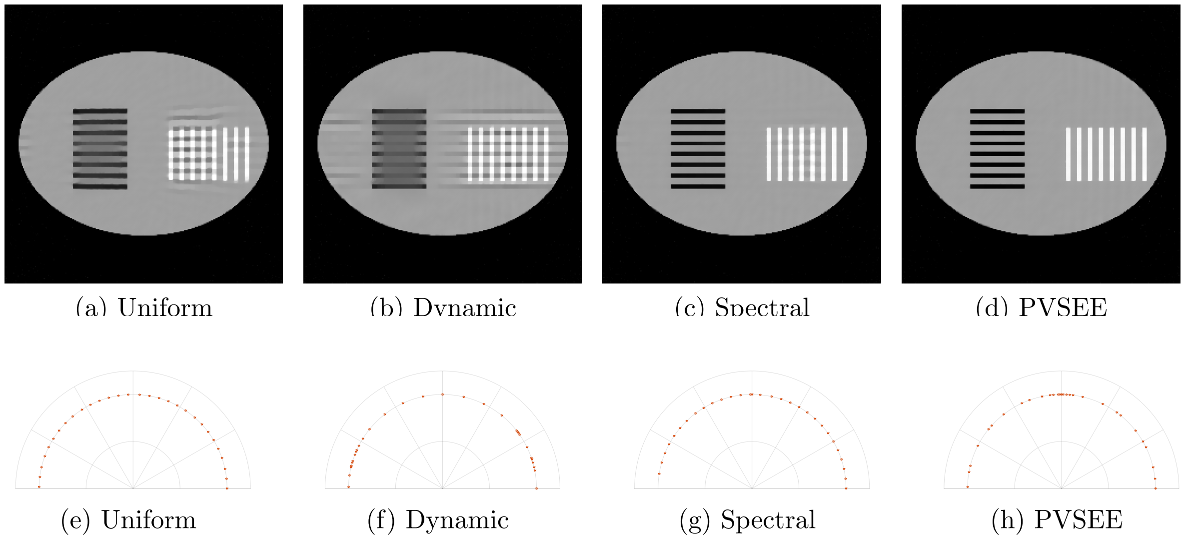

Figure 11: Results of projection view selection methods for Strips phantom from noisy projections ($M = 15$, $V = 30$).

Table 3: Quantitative evaluation (PSNR, SSIM) of projection view selection for Strips phantom on noisy projections.

Phantom	Index	Uniform	Dynamic	Spectral	PVSEE
Strips	PSNR	25.99	22.89	35.96	**38.15**
256×256	SSIM	0.9423	0.8301	0.9821	**0.9855**

To test the robustness of the proposed PVSEE against noise level change, we further performed two additional experiments at noise level $I_0 = 5\times10^5$ and $I_0 = 1\times10^5$, respectively. Reconstructed images from projections by the proposed PVSEE and comparative algorithms from noisy data at two different noise levels are shown in Fig. 12. From left to right, the four columns show the results by Uniform, Dynamic, Spectral and PVSEE, respectively. From top to bottom, the first two rows and the last two rows show the results at the noise level of $I_0 = 5 \times 10^5$ and $I_0 = 1 \times 10^5$, respectively. The competing methods Uniform, Dynamic and Spectral introduce more blurring and streak artifacts with the increasing noise level, while PVSEE can still recover white vertical strips nearly perfect. Taking a look at the the selected projection views illustrated in Fig. 12(e)-(h) and Fig. 12(m)-(p) at different noise levels, it is easy to observe that only PVSEE selects more projection views around 90° regardless of the noise levels, while all the competing methods fail to do so. This validates the robustness of PVSEE against noise levels. The quantitative indices listed in Table 4 agree well with above conclusion.

Table 4: Quantitative evaluation (PSNR, SSIM) of projection view selection for Strips phantom on noisy projections at different noise levels.

Noise level	Index	Uniform	Dynamic	Spectral	PVSEE
$I_0 = 5 \times 10^5$	PSNR	25.87	23.54	33.59	**36.07**
	SSIM	0.9132	0.8615	0.9507	**0.9577**
$I_0 = 1 \times 10^5$	PSNR	24.51	22.77	29.90	**31.10**
	SSIM	0.8342	0.7876	0.8765	**0.8881**

The second test is with the Shepp-Logan phantom without obvious preferential directions, as shown in Fig. 13(a). The scanning geometry is configured as follows: fan-beam source, the distance from the X-ray source to the object center is 311.49 mm, and the distance from the X-ray source to the detector is 697.88 mm. There are 512 detectors per view, each with a unit length of 0.127 mm. For noisy cases, Poisson noise with a photon count of 1×10^6 is introduced.

Since this phantom exhibits no obvious preferential directions, the desired projection views distribution should be near uniform. The original projection views set consists of $M = 10$ uniformly spaced angles, which is then expanded to $V = 15$ projection views by applying the views selection algorithms.

The results are illustrated in Fig. 14. At a first glance, all algorithms produce quite similar reconstructions which could be told from the first line of Fig. 14. A closer examination at the zoomed-in images from the second line, however, reveals the differences. All selection algorithms produce more consistent reconstructions than the uniform sampling scheme. If one checks the vicinity of the white edge, it's easy to conclude that the proposed PVSEE algorithm performs the best since it introduces almost no jagged artifacts, which are easy to be identified for competing algorithms. As stated, the Shepp-Logan phantom exhibits no obvious preferential directions. However, we indeed know that it might have weak preferential directions that are not easy to be recognized. It's interesting to notice that, by examining the last line of Fig. 14, the Spectral algorithm agrees well with the Uniform scheme, which suggests that the phantom should demonstrate no preferential directions. The Dynamic algorithm identifies two weak preferential directions near 120° and 240°, while the proposed

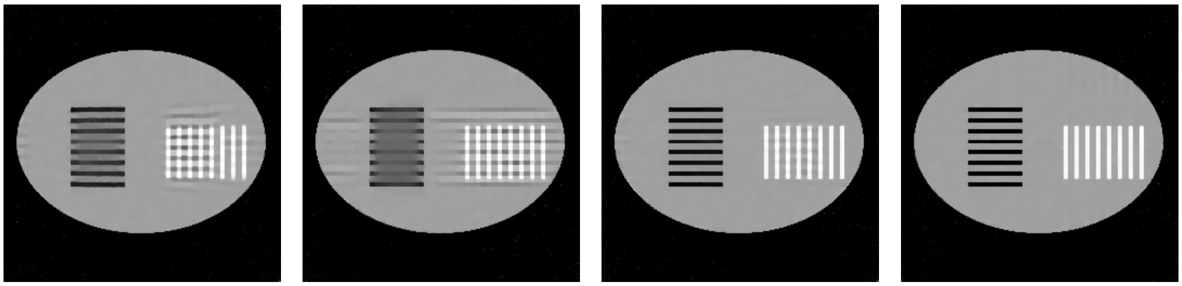

(a) Uniform, $I_0 = 5 \times 10^5$ (b) Dynamic, $I_0 = 5 \times 10^5$ (c) Spectral, $I_0 = 5 \times 10^5$ (d) PVSEE, $I_0 = 5 \times 10^5$

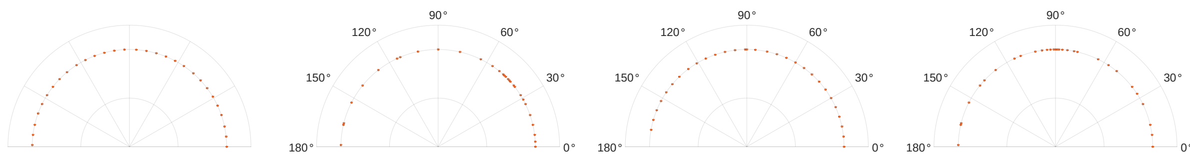

(e) Uniform, $I_0 = 5 \times 10^5$ (f) Dynamic, $I_0 = 5 \times 10^5$ (g) Spectral, $I_0 = 5 \times 10^5$ (h) PVSEE, $I_0 = 5 \times 10^5$

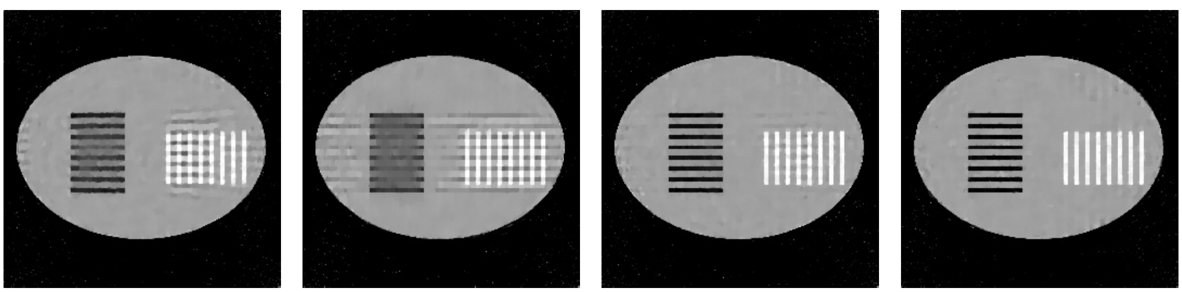

(i) Uniform, $I_0 = 1 \times 10^5$ (j) Dynamic,$I_0 = 1 \times 10^5$ (k) Spectral, $I_0 = 1 \times 10^5$ (l) PVSEE, $I_0 = 1 \times 10^5$

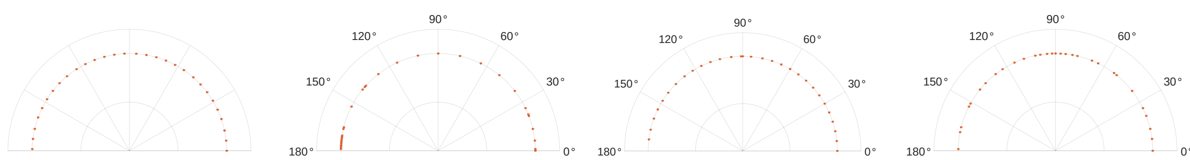

(m) Uniform,$I_0 = 1 \times 10^5$ (n) Dynamic,$I_0 = 1 \times 10^5$ (o) Spectral,$I_0 = 1 \times 10^5$ (p) PVSEE, $I_0 = 1 \times 10^5$

Figure 12: Results of projection view selection methods for Strips phantom from noisy projections at different noise levels. From up to bottom, the first two rows show the reconstructions and selected projection views distributions at $I_0 = 5 \times 10^5$ and the last tow rows show the results at $I_0 = 1 \times 10^5$.

(a) Phantom (b) SART, full data (c) SART, sparse-view data

Figure 13: (a) The Shepp-Logan phantom. (b) SART reconstruction from 360 views (10 iterations, noisy), (c) SART reconstruction from 15 views (10 iterations, noisy). The grayscale window is set to [0, 0.6].

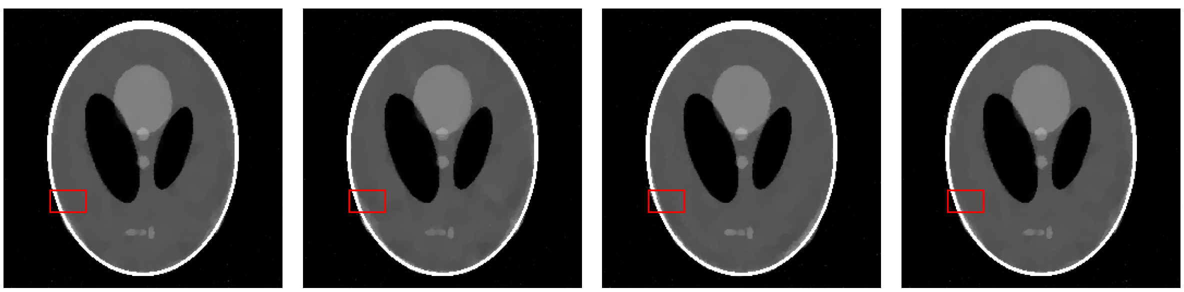

(a) Uniform (b) Dynamic (c) Spectral (d) PVSEE

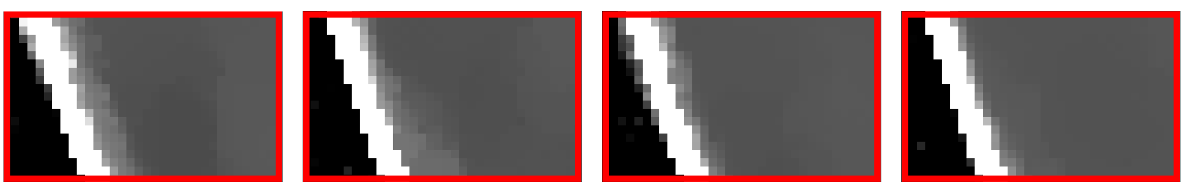

(e) Zoomed-in of (a) (f) Zoomed-in of (b) (g) Zoomed-in of (c) (h) Zoomed-in of (d)

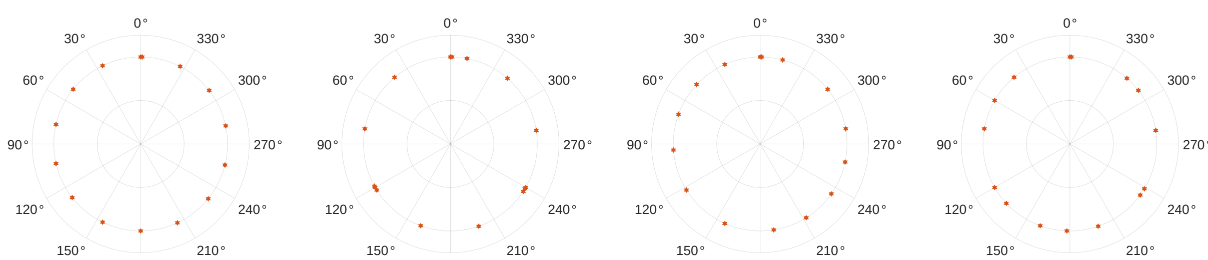

(i) Uniform (j) Dynamic (k) Spectral (l) PVSEE

Figure 14: Results of projection view selection methods for Shepp-Logan phantom from noisy projections ($M = 10$, $V = 15$).

PSVEE algorithm identifies just one (weak) preferential direction near 240°. Since PSVEE produces better reconstruction, the preferential direction near 120° might be a false alarm.

The quantitative indices listed in Table 5 confirm that, while the Dynamic and Spectral algorithms demonstrate apparent advantages over the Uniform sampling scheme, still the proposed PVSEE wins by a significant margin against all competing algorithms.

Table 5: Quantitative evaluation (PSNR, SSIM) of projection view selection for Shepp-Logan phantom on noisy projections.

Phantom	Index	Uniform	Dynamic	Spectral	PVSEE
Shepp-Logan	PSNR	30.52	33.61	34.36	**35.02**
256 × 256	SSIM	0.9694	0.9785	0.9832	**0.9833**

The third test is with a shoulder medical phantom with intricate edge and gray value distributions, as shown in Fig. 15 (a). The fan-beam scanning geometry is configured as follows: the distance from the X-ray source to the object center is 500 mm, and the distance from the X-ray source to the detector is 1000 mm. There are 1024 detectors per view, each with a unit length of 1.38 mm. The projections are acquired at dose of a photon count of $I_0 = 1 \times 10^6$. The number of initial uniform spaced projection views M is 30, which is then expanded to $V = 60$ projection views by employing PVSEE.

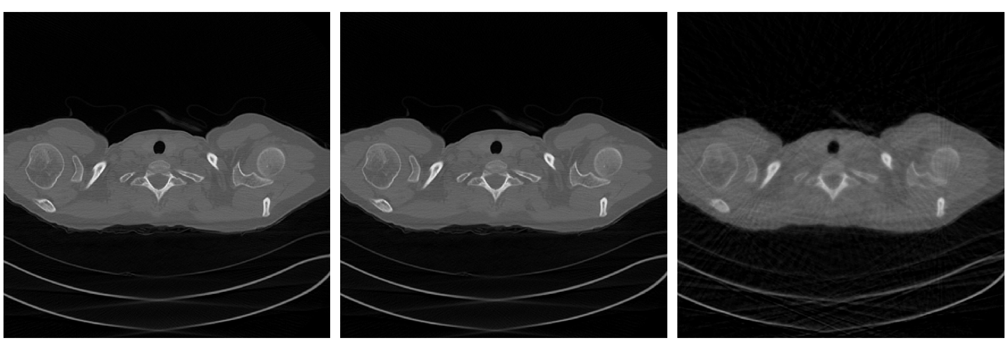

(a) Phantom (b) SART, full data (c) SART, sparse-view data

Figure 15: (a) The medical phantom, (b) Full angle SART reconstruction (10 iterations, noisy), (c) SART reconstruction from 60 views (10 iterations, noisy). The grayscale window is set to [0, 1].

The reconstructed results are illustrated in Fig. 16. At first sight, all algorithms produce very similar reconstructions, as seen in the top row of Fig. 16. When checking the zoomed-

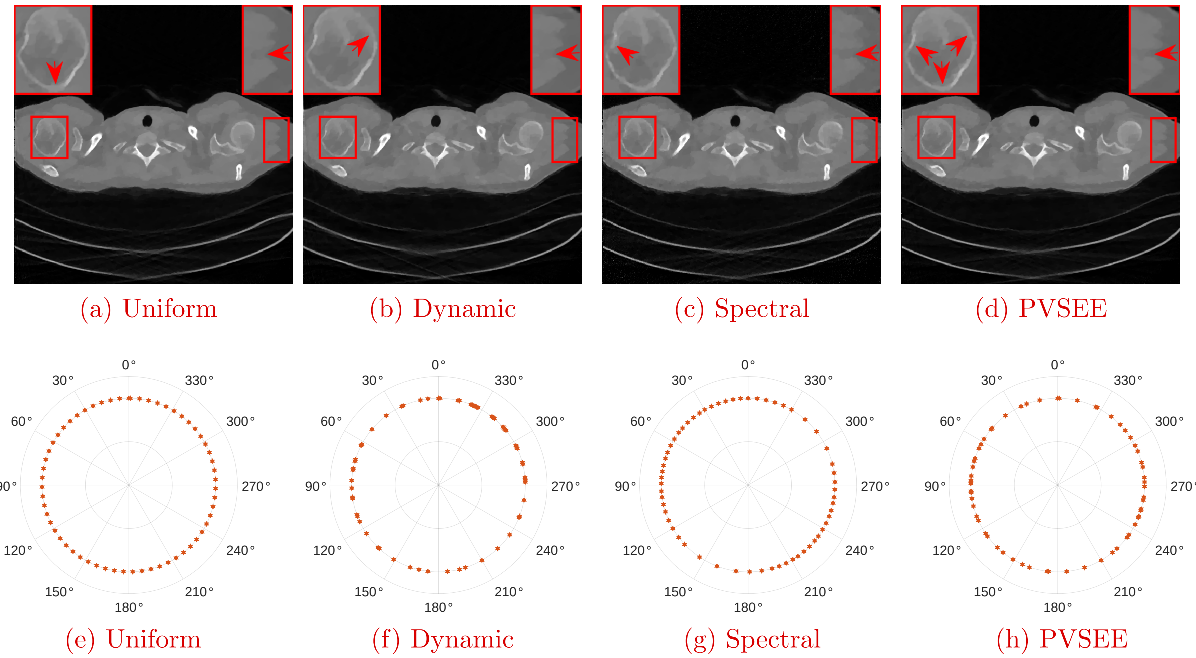

Figure 16: Results of projection view selection methods for the medical phantom from noisy projections (M = 30, V =60). The grayscale window is set to [0, 0.8].

in areas within the red rectangles, it can be told that the left bone boundaries and right soft-tissue boundaries with the proposed PVSEE, indicated by the red arrows, closely match the reference image. In contrast, the competing algorithms, Uniform, Dynamic and Spectral, exhibit blurring or deformation. Considering that the edge distribution of the shoulder phantom does not exhibit obvious orientations, only weak preferential directions that not easily noticed might be identified. By examining the selected projection views shown in Fig. 16(f)-(h), one can see that the Spectral algorithm fails to identify any preferential directions, the Dynamic algorithm detects weak preferential directions, and the proposed PVSEE algorithm identifies several other weak preferential directions. Since PVSEE achieves better reconstruction, one can conclude that the proposed PVSEE can effectively and correctively identify weak preferential directions in this complex phantom, while competing algorithms fail to do so. Similar conclusion can be made from the quantitative indices listed in Table 6.

III.B.2. Performance test on real data

In this subsection, to test the potential capability of our method in practical applications, experiments are carried out on real data. For this test, complete projection data are initially

Table 6: Quantitative evaluation (PSNR, SSIM) of projection view selection for the medical phantom on noisy projections.

Phantom	Index	Uniform	Dynamic	Spectral	PVSEE
Medical image	PSNR	34.58	33.30	33.33	**35.27**
512×512	SSIM	0.8882	0.8795	0.8252	**0.8971**

acquired through full angular scanning. The SART algorithm is then employed on this complete data to construct a reference image. For simplicity, we deal with just one layer (the central slice) of the reconstructed image in the experiment.

The first test involves a real flat object with a high length-width ratio, as shown in Fig. 17(a), which is reconstructed from real full scanning data acquired by the CT device located in our lab. The CT system consisted of a YXLON-FXE-225.48 X-ray source and a Varian PS2520V flat panel detector. Detailed system and geometrical scanning parameters are listed in Table 7. The reconstructed images are originally size of 480×480, however, for

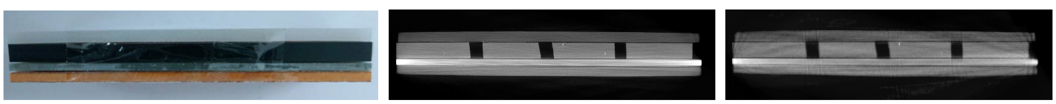

(a) Phantom (b) SART, full data (c) SART, sparse-view data

Figure 17: (a) Photograph of the flat object, (b) the reference image reconstructed from the full-angle data (SART, 10 iterations), (c) SART reconstruction from 30 views (10 iterations). The grayscale window is of [0, 0.12].

Table 7: System and geometrical scanning parameters.

Parameter	Value
Tube voltage	140kV
Current	160mA
Scanning range	360°
Scanning angular interval	1°
Number of detector units	960
Detector unit width	0.254mm
X-ray source to the rotation center distance	311.49mm
X-ray source to detector distance	697.88mm
Reconstructed image size	480×480

better illustration, they are clipped to 132×480. The original projection views set consists of

$M = 10$ uniformly spaced angles drawn from the full projection data, which is then expanded to $V = 30$ projection views by applying the views selection algorithms. Fig. 17(b) shows the SART reconstruction with 10 iterations from full angle projections to act as a reference and Fig. 17(c) displays the SART reconstruction with 10 iterations from uniformly sampled 30 projection views.

The reconstructed results alongside the distribution of selected projection views are shown in Fig. 18. Both the Dynamic and Spectral schemes manage to recover the small structure indicated by the red arrows, but they failed to recover the horizontal edges indicated by the red arrows. In contrast, the proposed PVSEE scheme seems to be able to preserve the small structure while recovering the horizontal edges.

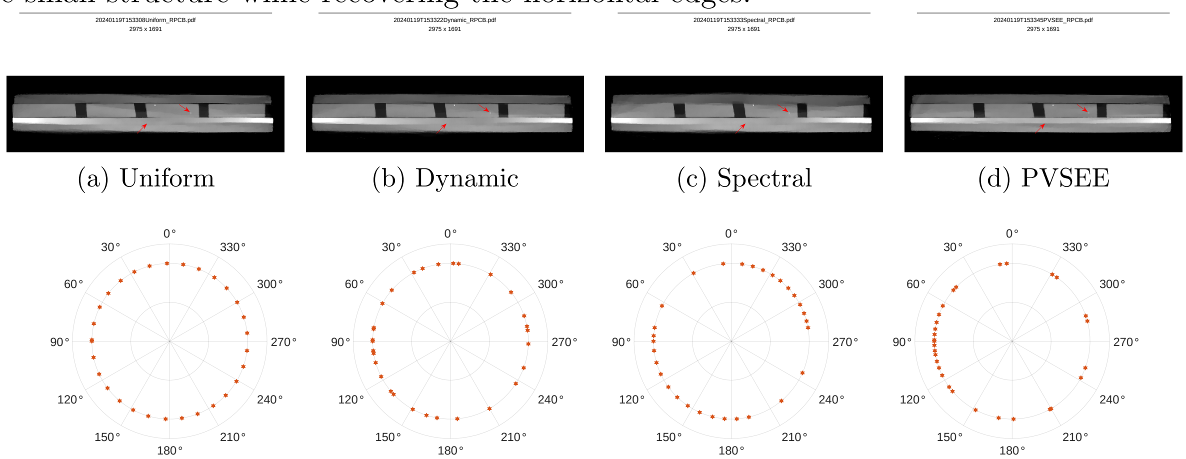

(a) Uniform (b) Dynamic (c) Spectral (d) PVSEE

(e) Uniform (f) Dynamic (g) Spectral (h) PVSEE

Figure 18: Results of projection view selection methods for the PCB real data (M = 15, V = 30).

Compared to the uniform sampling scheme, projection views selected by all competing algorithms demonstrate some kind of concentration around 90° (corresponding to the horizontal direction), as illustrated in Fig. 18(e)-(h). However, a closer inspection reveals differences. It's interesting to notice that the selected projection views by the competing algorithms demonstrate different concentration patterns. Both the Dynamic scheme and the Spectral scheme result in skewed concentration, i.e. not perfectly around 90°. As a comparison, the proposed PSVEE gives very symmetric and dense concentration around 90°. This indicates that PSVEE could more accurately identify the preferential directions than the competing algorithms. The quantitative indices listed in Table 8 show that the proposed PVSEE algorithm wins a large margin in terms of both PSNR and SSIM. This agrees well with the above analysis.

Table 8: Quantitative evaluation (PSNR, SSIM) of projection view selection on real PCB data.

Phantom	Index	Uniform	Dynamic	Spectral	PVSEE
PCB	PSNR	37.27	38.02	37.13	**39.79**
480×480	SSIM	0.9797	0.9806	0.9794	**0.9814**

The second test utilizes real projection data of a carved cheese from an open-access source[37], as shown in Fig. 19(a). As explained in[37], the reconstruction is carried out using data from a custom-built CT device at the University of Helsinki, and the CT system employs the X-ray source (XTF5011) and a Hamamatsu Photonics C7942CA-22 flat panel detector. Other system and geometrical scanning parameters are listed in Table 9. As a reference, the full angle reconstruction (SART, 10 iterations) is shown in Fig. 19(b). Since the object

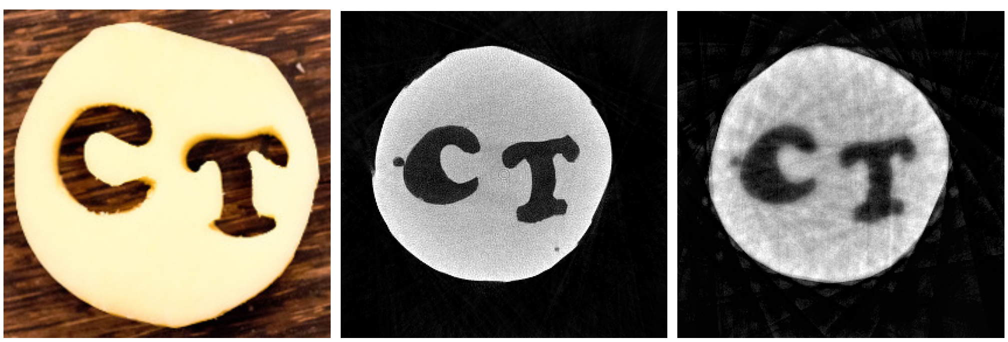

(a) Phantom (b) SART, full data (c) SART, sparse-view data

Figure 19: (a) Photograph of the carved cheese, (b) the reference image reconstructed from the full-angle data (SART, 10 iterations), (c) SART reconstruction from 20 views (10 iterations). The grayscale window is of [0, 0.2].

under inspection has simple structure, we set the budget for the number of total projection views to be $V = 20$. The original projection views set consists of $M = 10$ uniformly spaced projection views, which is then expanded to $V = 20$ projection views by applying the views selection algorithms. The SART reconstruction (10 iterations) from uniformly sampled 20 projection views is shown in Fig. 19(c).

This phantom has no preferential directions and the Uniform scheme should be near optimal for placing the projection views. Fig. 20 shows the reconstructed images from selected

Table 9: System and geometrical scanning parameters.

Parameter	Value
Tube voltage	40kV
Current	1mA
Scanning range	360°
Scanning angular interval	1°
Number of detector units	560
Detector unit width	0.2mm
X-ray source to the rotation center distance	404.3mm
X-ray source to detector distance	547.8mm
Reconstructed image size	280 × 280

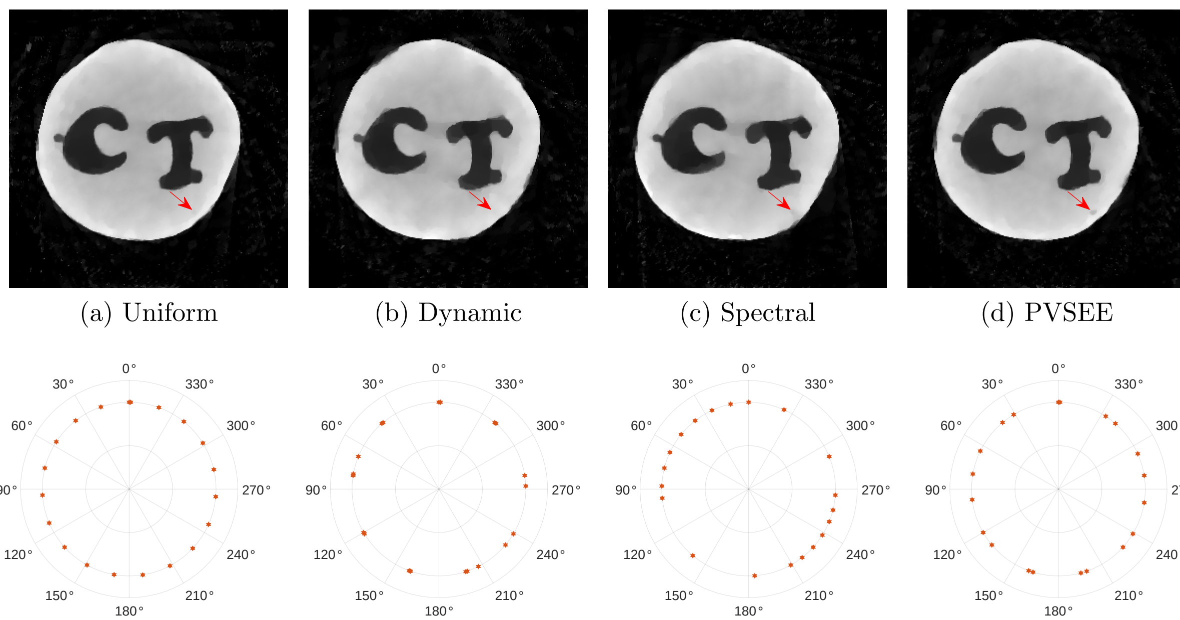

(a) Uniform (b) Dynamic (c) Spectral (d) PVSEE

(e) Uniform (f) Dynamic (g) Spectral (h) PVSEE

Figure 20: Results of projection view selection methods for the cheese real data ($M = 10$, $V = 20$).

20 projections by different selection methods, together with the corresponding views distributions. From the first line, all competing algorithms produce quite similar reconstructions from a global view. A closer inspection, especially in the vicinity indicated by the arrows, one can see that the small structure pointed to by the arrow is completely lost for the Dynamic algorithm, diminished or blurred to be almost non-recognizable for the Uniform and SFS schemes, while PVSEE preserves the structure quite well. When checking the projection views distribution illustrated in the second row of Fig. 20, we can see that the proposed

PVSEE results in a distribution closest to the uniform one, which is desirable since the scanned object has no preferential directions. In fact, simple computations show that, the maximum angular intervals for the four competing algorithms, i.e. the Uniform, Dynamic, Spectral and the proposed PVSEE, are 19°, 40°, 44° and 31°, respectively, which suggests that the proposed PVSEE behaves the best since its largest angular interval is closest to that of the Uniform scheme. The above analysis and conclusion can be further validated by com-

Table 10: Quantitative evaluation (PSNR, SSIM) of projection view selection on real Cheese data.

Phantom	Index	Uniform	Dynamic	Spectral	PVSEE
Cheese	PSNR	27.02	26.33	26.56	**27.01**
280×280	SSIM	0.8965	0.8930	0.8916	**0.8966**

paring the quantitative indices listed in Table 10, where the PSNR and SSIM values show that the proposed PVSEE takes an advantage over the Dynamic and Spectral algorithms, and achieves almost same performance compared to the Uniform scheme.

IV. Discussion

In this section, we will further explore the proposed PSVEE algorithm, including the choice for the initial set of projection views, proposing a variant of PSVEE for better utilizing prior information about preferential directions and the possible application scenarios.

IV.A. The initial set of projection views

As previously mentioned, in the absence of prior information, the initial M projection views can be uniformly distributed. In certain applications, the preferential directions of the scanned object could be inferred before scanning, e.g. the CAD model for the scanned object is available. This prior information can be incorporated into the selection of the initial set of projection views by specifying more projection views around the preferential directions, which could significantly improve the effectiveness of projection views selection.

When prior information is not available, uniform sampling is a reasonable choice to specify the initial set of M projection views. How different choices of M affect the reconstruction quality? To explore the stability and limits of the proposed method under the condition of different initial uniform sampling angles M, we conducted experiments on the simulated Strips phantom shown in Fig. 10(a) with $M = 3, 7, 11, 15, 19, 23, 27$ and the budget for total number of projection views $V = 30$. The scan geometry and noise level settings align with those specified in section III.B.1..

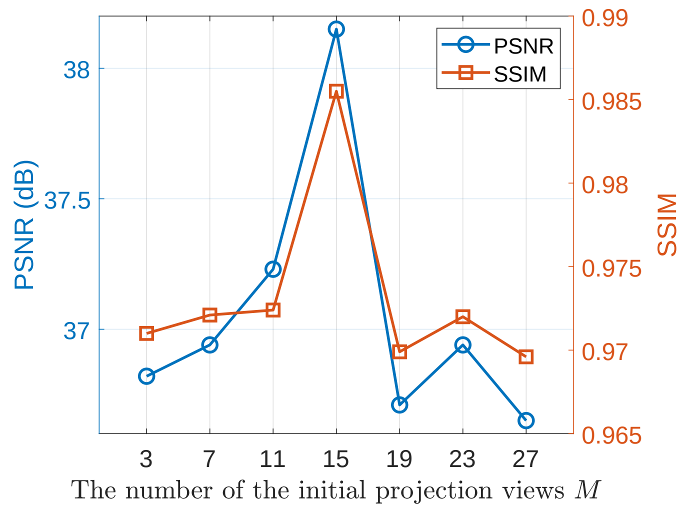

Figure 21: The PSNR and SSIM results of the experiments with different numbers of initial projection view on the Strips phantom at the noise level of $I_0 = 1 \times 10^6$.

Fig. 21 shows the line charts of PSNR and SSIM against the size of initial uniform sampling angles M. As shown in Fig. 21, with the increase of the number of initial uniform sampling angles M, PSNR and SSIM show a trend of first increasing and then decreasing, and reach the highest value when $M = 15$. This phenomenon coincides well with our expectations. A too small M will give a initial bad quality image, so PVSEE will be fed with "wrong" information and the determined projection views shall not be so "informative", which finally affect the reconstruction quality. On the other hand, a too large M will limit PVSEE to demonstrate its power and advantages since there are no much work left for it to do. From the line chart, one can also observe a nonsymmetric askew pattern: for both the PSNR and SSIM curves, the left part is higher than the right part. This actually indicates the effectiveness and robustness of PVSEE: when fed with "wrong" information, PVSEE can still identify relatively informative projection views such that the reconstructed image is still of higher quality than that with uniform sampling.

IV.B. The recursive variant of PVSEE method

As outlined in **Algorithm 1**, when the budget for the number of projection views is V and an initial set of M projection views is specified, PVSEE selects $V-M$ projection views all at once. This all-at-once strategy might be sub-optimal, particularly when the initial set of M projection views is very sparsely distributed. To mitigate this possible issue, we propose a variant of the proposed PSVEE algorithm, named recursive PSVEE (RPSVEE) algorithm, which selects the $V-M$ views by a recursive strategy, i.e. the views are added in small batches, one by one. In this way, even if the initial set of M projection views does not contain preferential directions, they should be revealed during the recursive procedure if the object under scanning indeed possesses preferential directions. The variant RPSVEE algorithm is easy to implement, only involving an outer loop over the partition $\{V_i\}_{i=1}^{N}$ of $V-M$, see **Algorithm 2** for details.

Algorithm 2: Recursive projection view selection algorithm based on error equidistribution (RPVSEE)

Input: Initial M projection views $\{\theta_i\}_{i=1}^{M}$, the number of target projection views V, subset partitions V_1, V_2, $\cdots$, V_N, $\sum_{i=1}^{N} V_i = V - M$

Initialize: $\Theta \leftarrow \{\theta_i\}_{i=1}^{M}, \Theta'_0 \leftarrow \Theta$

for $i := 1$ **to** N **do**

  # **Step 1**: estimate the projection error

  Acquiring new projection data $p_{[\Theta'_{i-1}]}$ for the views in Θ'_{i-1}

  Performing image reconstruction from projection data $p_{[\Theta]}$ by $u \leftarrow$ **Reconstruction**$(p_{[\Theta]})$

  Estimating the projection errors and generating the error curve $\mathcal{E}(\theta)$ by applying (3)

  # **Step 2**: select new V_i projection views $\Theta'_i = \{\theta'_j\}_{j=1}^{V_i}$ by applying the error equidistribution law (4)

  Including the selected views Θ'_i into the acquired set of projection views by $\Theta \leftarrow \Theta \cup \Theta'_i$

end for

Step 3: achieve the final reconstruction

Performing image reconstruction by $u' \leftarrow$ **Reconstruction**$(p_{[\Theta]})$

Output: u'

To validate the effectiveness of the RPVSEE variant, experiments were conducted using the simulated PCB phantom shown in Fig. 6(a). The scan geometry and noise level settings align with those specified in section III.B.1.. As mentioned above, this phantom possesses preferential directions at 0° and 90°. For both PVSEE and RPVSEE, the parameters are set to $M = 4$, $V = 30$, and the initial 4 projection views are uniformly distributed. For the PVSEE algorithm, 26 projection views are determined all at once based on the error curve calculated by the initial 4 projection views, while for the RPVSEE algorithm, the 26 projection views that need to be determined are divided into 5 groups which contain $\{6, 5, 5, 5, 5\}$ projection views, respectively. So, for RPVSEE algorithm, it shall firstly add 6 projection views, then 5 projection views are added, and so on, until reaching the budget of 30 projection views.

The reconstructed results as well as the determined 30 projection views are illustrated in Fig. 22. Clearly, RPVSEE results in much better reconstruction compared to PSVEE. The distributions of the selected projection views shown are illustrated in Fig. 22(c) and (d). Note that different marker shapes are employed to represent different sets of selected projection views during RPVSEE's recursive selection process.

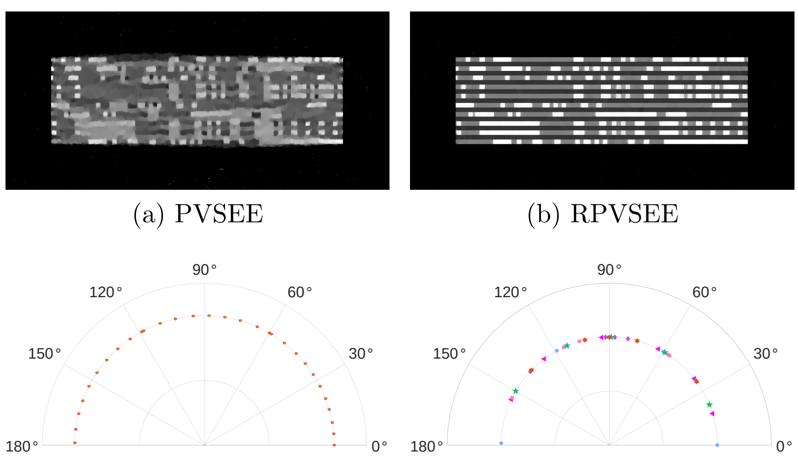

(a) PVSEE (b) RPVSEE

(c) PVSEE (d) RPVSEE

Figure 22: Results of projection view selection methods for PCB phantom from noisy projections ($M = 4$, $V = 30$).

It's obvious to tell that PVSEE leads to almost uniform distribution and fails to reveal the preferential direction. This behavior is understandable since the initial 4 projection views contain no information about the preferential directions. On the contrary, RPVSEE successfully identifies the preferential direction in the set of finally selected projection views since concentration of views around the preferential direction 90° is easy to be recognized.

IV.C. The application scenarios

The prototypes of PVSEE and RPVSEE algorithms could be easily adapted to real applications. It should be emphasized that the proposed algorithms allow for the selecting-while-reconstructing mode, i.e. once a new view is selected, the scanning is performed for this new view, and the new acquired projection data is then used to update the image, based on which new projection views are again selected, and so on. When the total number of projection views reaches the planned budget, the iterative reconstruction procedure can proceed, if necessary, without selecting new views.

Compared to the reconstruction procedure, the view selection procedure is much faster, thus the waiting time between consecutive scannings can be neglected. So, one can think that the proposed algorithm identifies informative projection views in real-time. This capability is essential for applying the proposed methods to current medical CT imaging systems, in which the X-ray source can not be stopped and always produces photons during the whole scanning process. We believe that manufactures would be willing to adapt their scanning system once they confirm that nonuniform scanning worth of it. As an example, the emerging stationary CT system[38,39] consists of multiple sources and detectors, and each pair of source and detector can be separately controlled for scanning. In this scenario, the proposed algorithm could be applied without introducing any extra overhead, compared to traditional sequential scanning protocol.

In certain applications, the objects under scanning share similar shape and structure. In this scenario, the informative projection views could be determined once by experiments and then fixed for subsequent examinations. This includes CT imaging needs for teeth, head, chest, etc, and it also includes industrial CT applications like battery examination.

V. Conclusion

Motivated by two key observations of projection error's behaviors, we have introduced the idea of error equidistribution for selecting informative projection views. To our knowledge, this marks the first instance of utilizing projection errors to serve as an indicator of view importance in optimizing the selection of projection views.

Compared to existing algorithms, the proposed PVSEE algorithm produces very competitive or superior results which are verified by extensive numerical experiments. Besides, with proper programming, e.g. each implementation of the reconstruction operator could be fed with only newly added projection views and the current reconstructed image, the time consumption of the PVSEE algorithm shall be comparable to those of traditional popular methods like SART, thus our PVSEE suits well to time-critical real applications.

Acknowledgment

This work was supported by Beijing Natural Science Foundation (No. Z210003), National Natural Science Foundation of China (NSFC) (62101056, 61971292), National Key Research and Development Program of China, Grant/Award Number (2020YFA0712200) and key research project of the Academy for Multidisciplinary Studies, Capital Normal University. The authors are also grateful to the Beijing Higher Institution Engineering Research Center of Testing and Imaging as well as the Beijing Advanced Innovation Center for Imaging Technology for funding this research work.

References

[1] R. A. Brooks and G. D. Chiro, Principles of computer assisted tomography (CAT) in radiographic and radioisotopic imaging, Physics in Medicine & Biology **21**, 689 (1976).

[2] J. S. Jorgensen, E. Y. Sidky, and X. Pan, Quantifying Admissible Undersampling for Sparsity-Exploiting Iterative Image Reconstruction in X-Ray CT, IEEE Transactions on Medical Imaging **32**, 460–473 (2013).

[3] D. P. Frush, L. F. Donnelly, and N. S. Rosen, Computed tomography and radiation risks: what pediatric health care providers should know, Pediatrics **112**, 951–957 (2003).

[4] E. Y. Sidky and X. Pan, Report on the AAPM deep-learning sparse-view CT grand challenge, Medical Physics **49**, 4935–4943 (2022).

[5] E. Y. Sidky, C.-M. Kao, and X. Pan, Accurate image reconstruction from few-views and limited-angle data in divergent-beam CT, 2009.

[6] Z. Zhang, B. Chen, D. Xia, E. Y. Sidky, and X. Pan, Directional-TV algorithm for image reconstruction from limited-angular-range data, Medical Image Analysis **70**, 102030 (2021).

[7] L. Yu, X. Liu, S. Leng, J. M. Kofler, J. C. Ramirez-Giraldo, M. Qu, J. Christner, J. G. Fletcher, and C. H. McCollough, Radiation dose reduction in computed tomography: techniques and future perspective, Imaging in medicine **1**, 65 (2009).

[8] I. G. Kazantsev, Information content of projections, Inverse Problems **7**, 887 (1991).

[9] L. Varga, P. Balázs, and A. Nagy, Direction-dependency of binary tomographic reconstruction algorithms, Graphical Models **73**, 365–375 (2011), Computational Modeling in Imaging Sciences.

[10] Y. Lu, H.-P. Chan, J. Wei, M. Goodsitt, P. L. Carson, L. Hadjiiski, A. Schmitz, J. W. Eberhard, and B. E. H. Claus, Image quality of microcalcifications in digital breast tomosynthesis: Effects of projection-view distributions, Medical Physics **38**, 5703–5712 (2011).

[11] G. L. Zeng, A filtered backprojection MAP algorithm with nonuniform sampling and noise modeling, Medical Physics **39**, 2170–2178 (2012).

[12] H. Xie, T. Niu, Y. Ren, Y. Yang, and X. Tang, MO-FG-204-08: Optimization-Based Image Reconstruction From Unevenly Distributed Sparse Projection Views, Medical Physics **42**, 3570–3571 (2015).

[13] G. Placidi, M. Alecci, and A. Sotgiu, Theory of Adaptive Acquisition Method for Image Reconstruction from Projections and Application to EPR Imaging, Journal of Magnetic Resonance, Series B **108**, 50–57 (1995).

[14] M. Venere, H. Liao, and A. Clausse, A genetic algorithm for adaptive tomography of elliptical objects, IEEE Signal Processing Letters **7**, 176–178 (2000).

[15] E. T. Quinto, Singularities of the X-Ray Transform and Limited Data Tomography in $\mathbb{R}^2$ and $\mathbb{R}^3$, SIAM Journal on Mathematical Analysis **24**, 1215–1225 (1993).

[16] K. Mueller, Selection of optimal views for computed tomography reconstruction, 2011, US Patent App. 12/842,274.

[17] Z. Zheng and K. Mueller, Identifying sets of favorable projections for few-view low-dose cone-beam CT scanning, in *11th International meeting on fully three-dimensional image reconstruction in radiology and nuclear medicine*, pages 314–317, Citeseer, 2011.

[18] M. A. Haque, M. O. Ahmad, M. N. S. Swamy, M. K. Hasan, and S. Y. Lee, Adaptive Projection Selection for Computed Tomography, IEEE Transactions on Image Processing **22**, 5085–5095 (2013).

[19] K. J. Batenburg, W. J. Palenstijn, P. Balázs, and J. Sijbers, Dynamic angle selection in binary tomography, Computer Vision and Image Understanding **117**, 306–318 (2013), Special issue on Discrete Geometry for Computer Imagery.

[20] A. Dabravolski, K. J. Batenburg, and J. Sijbers, Dynamic angle selection in X-ray computed tomography, Nuclear Instruments and Methods in Physics Research Section B: Beam Interactions with Materials and Atoms **324**, 17–24 (2014), 1st International Conference on Tomography of Materials and Structures.

[21] G. Lékó and P. Balázs, Sequential Projection Selection Methods for Binary Tomography, in *Computational Modeling of Objects Presented in Images. Fundamentals, Methods, and*

Applications, edited by R. P. Barneva, V. E. Brimkov, P. Kulczycki, and J. M. R. S. Tavares, pages 70–81, Cham, 2019, Springer International Publishing.

[22] V. Bussy, C. Vienne, and V. Kaftandjian, Fast algorithms based on Empirical Interpolation Methods for selecting best projections in Sparse-View X-ray Computed Tomography using a priori information, NDT & E International **134**, 102768 (2023).

[23] J. J. Lifton and K. Y. Poon, IntelliScan: Improving the quality of x-ray computed tomography surface data through intelligent selection of projection angles, Journal of X-Ray Science and Technology **31**, 119–129 (2023), Publisher: IOS Press.

[24] Z. Shen, Y. Wang, D. Wu, X. Yang, and B. Dong, Learning to scan: A deep reinforcement learning approach for personalized scanning in CT imaging, Inverse Problems and Imaging **16**, 179–195 (2022).

[25] L. Yang, R. Ge, S. Feng, and D. Zhang, Learning Projection Views for Sparse-View CT Reconstruction, in *Proceedings of the 30th ACM International Conference on Multimedia*, MM '22, page 2645–2653, New York, NY, USA, 2022, Association for Computing Machinery.

[26] D. A. Anderson, Equidistribution schemes, poisson generators, and adaptive grids, Applied Mathematics and Computation **24**, 211–227 (1987).

[27] K. Chen, Error Equidistribution and Mesh Adaptation, SIAM Journal on Scientific Computing **15**, 798–818 (1994).

[28] P. R. Eiseman, Alternating direction adaptive grid generation, AIAA Journal **23**, 551–560 (1985).

[29] G. F. Carey and H. T. Dinh, Grading Functions and Mesh Redistribution, SIAM Journal on Numerical Analysis **22**, 1028–1040 (1985).

[30] G. Beckett and J. Mackenzie, On a uniformly accurate finite difference approximation of a singularly perturbed reaction–diffusion problem using grid equidistribution, Journal of Computational and Applied Mathematics **131**, 381–405 (2001).

[31] I. G. Kazantsev, Information content of projections in few-views tomography, in *Analytical Methods for Optical Tomography*, edited by G. G. Levin, volume 1843, pages 62 – 65, International Society for Optics and Photonics, SPIE, 1992.

[32] L. Varga, P. Balazs, and A. Nagy, Projection Selection Dependency in Binary Tomography, Acta Cybernetica **20**, 167–187 (2011).

[33] Z. Wang, A. Bovik, H. Sheikh, and E. Simoncelli, Image quality assessment: from error visibility to structural similarity, IEEE Transactions on Image Processing **13**, 600–612 (2004).

[34] W. van Aarle, W. J. Palenstijn, J. De Beenhouwer, T. Altantzis, S. Bals, K. J. Batenburg, and J. Sijbers, The ASTRA Toolbox: A platform for advanced algorithm development in electron tomography, Ultramicroscopy **157**, 35–47 (2015).

[35] Z. Wang, E. P. Simoncelli, and A. C. Bovik, Multiscale structural similarity for image quality assessment, The Thirty-Seventh Asilomar Conference on Signals, Systems & Computers, 2003 **2**, 1398–1402 Vol.2 (2003).

[36] S. Zhao, D. Xia, and X. Zhao, A fast image reconstruction method for planar objects CT inspired by differentiation property of Fourier transform (DPFT), Inverse Problems **37**, 075001 (2021).

[37] T. A. Bubba, M. Juvonen, J. Lehtonen, M. März, A. Meaney, Z. Purisha, and S. Siltanen, Tomographic X-ray data of carved cheese, 2017.

[38] T. Zhang, Y. Xing, L. Zhang, X. Jin, H. Gao, and Z. Chen, Stationary computed tomography with source and detector in linear symmetric geometry: Direct filtered backprojection reconstruction, Medical Physics **47**, 2222–2236 (2020).

[39] Y. Xia, L. Zhang, Y. Xing, Z. Chen, and H. Gao, Generalized-equiangular geometry CT: Concept and shift-invariant FBP algorithms, Medical Physics **50**, 5150–5165 (2023).